Regularization Methods for Extracting Doppler Broadening From Hall Thruster Plasma

A. K. M. Mustafizur Rahman and Richard Branam

***Abstract*— Extracting Doppler broadening from laser-induced fluorescence (LIF) measurements is essential for determining species temperature in the plasma. The fluorescence signal is a convolution of many broadening effects of which Doppler broadening is the most significant, but several others contribute as well: collisional (pressure) broadening (particle-to-particle interactions), natural lifetime broadening, and power broadening. The process that extracts Doppler broadening is an *ill-posed* inverse problem. The regularization approach addresses the *ill-posed* problem to ensure a unique and stable solution with the best possible accuracy. This study reported the Xe II temperature by applying truncated singular value decomposition (TSVD) and Tikhonov regularization (zeroth, first and second-order) methods for deconvolution of Doppler broadening. Tikhonov first-order and TSVD employing the generalized cross-validation (GCV) method provide accurate reconstruction within 2.0%–8.0% of the actual measurements.**

***Index Terms*— Doppler broadening, hall thruster, laser-induced fluorescence (LIF), Tikhonov, truncated singular value decomposition (TSVD).**

I. Introduction

LASER-INDUCED fluorescence (LIF) is a popular, non-intrusive technique used to characterize the plasma of a Hall effect thruster (HET). A specific laser frequency associated with a particular electronic transition can increase the corresponding excited-state population. The excited-state species eventually returns to a ground/intermediate state, producing measurable fluorescence. The center frequency of the fluorescence is known, but the measured intensity is distributed over a small frequency range. The fluorescence signal is a result of several broadening and shifting effects, such as Doppler broadening, collisional (pressure) broadening (particle-to-particle interactions), natural lifetime broadening, and power broadening induced by laser irradiance. The optical spectrum is a full or partial blend of many different components which includes the above broadening effects as well as the contribution of hyperfine structure (Hfs) and isotope shift (IS). If a sufficiently high-resolution spectral apparatus is used, these many effects can be seen and resolved. The nucleus of an atom has a magnetic dipole moment related to the nuclear spin. The interaction of this magnetic dipole moment with the magnetic field created by the valence electrons results in energy level splitting known as Hfs. The differences in the mass and charge distribution of the nucleus shift the center frequency of the spectra up to 120 MHz, which is referred to as IS. Xenon has nine isotopes; seven isotopes have an even number of neutrons in the nucleus, which balances the relative nuclear spin (net spin is zero). However, xenon with an atomic mass of 129 and 131 (129_{Xe} and 131_{Xe}) has unpaired neutrons, resulting in non-zero nuclear spin and exhibiting Hfs. The constants associated with the magnetic dipole and electric quadrupole interaction allow us to determine the energy shift. Depending on the transition, this energy shift can be up to several GHz. External magnetic and electric fields contribute to additional spectral splitting known as Zeeman and Stark effects, but broadening due to these effects is significantly less than other types of broadening. The splitting and shifting effects contribute to the fluorescence spectrum, enabling the final spectrum to be broader.

Researchers have shown that each physical phenomenon can be mathematically characterized using distribution functions related to the physical properties of the plasma. The expected LIF line shape is then a convolution of all the physical phenomena, including the Stark and Zeeman effects, and can be expressed in the following equation:

$$\text{Fluorescence} = \text{Doppler} \otimes \text{Hfs} \otimes \text{pressure} \otimes \text{natural} \otimes \text{Stark} \otimes \text{Zeeman}. \quad (1)$$

The cross inside the circle ($\otimes$) represents the convolution operator, i.e., the fluorescence signal is a convolution associated with the Hfs, the Zeeman effect, the Stark effect, and broadening due to natural lifetime, pressure, and the Doppler effect. The species temperature characterizes the Doppler effect, which is often represented by a Boltzmann distribution. If the Doppler broadening of the LIF signal can be separated, the species' temperature can be determined. A deconvolution algorithm is necessary to extract Doppler broadening. Cedolin et al. [1] used a nonlinear optimization routine to fit computational spectra with measured spectra. However, the approach did not agree with the measured spectra over the entire range. Keefer et al. [2] applied a method similar to Cedolin et al. [1]. Smith [3] attempted to solve the inverse

Manuscript received 10 August 2022; accepted 4 March 2023. Date of publication 5 April 2023; date of current version 19 May 2023. This work was supported in part by the National Science Foundation (NSF) Established Program to Stimulate Competitive Research (EPSCoR) Connecting the Plasma Universe to Plasma Technology in Alabama (CPU2AL) under Grant OIA-1655280. The review of this article was arranged by Senior Editor S. Portillo. *(Corresponding author: A. K. M. Mustafizur Rahman.)*

The authors are with the Department of Aerospace Engineering and Mechanics, The University of Alabama, Tuscaloosa, AL 35487 USA (e-mail: arahman2@crimson.ua.edu; rdbranam@eng.ua.edu).

Color versions of one or more figures in this article are available at https://doi.org/10.1109/TPS.2023.3263375.

Digital Object Identifier 10.1109/TPS.2023.3263375

problem by developing several deconvolution approaches to separate the effects of different phenomena. The deconvolution processes amplified the noise, requiring additional smoothing techniques to obtain meaningful results. Hargus and Nakles [4] applied a zeroth-order (classical) Tikhonov algorithm with the L-curve method to the problem. Hargus and Nakles's approach reduced noise in the deconvolution but artificially narrowed the line shape and increased the maximum intensity by as much as 20%. The L-curve method for Tikhonov regularization tends to produce a slightly over-smoothed reconstruction. If the singular value decomposition (SVD) coefficients decay faster to zero such that the first few SVD components dominate the solution, the L-curve criteria may fail.

This study has reported truncated SVD (TSVD) and Tikhonov regularization techniques by means of the L-curve and generalized cross-validation (GCV) methods for singly ionized xenon (Xe II). The effort has included first- and second-order terms more accurately. The Tikhonov first-order and TSVD employing the GCV method provide reconstruction within 2.0%–8.% of the actual measurements.

II. Problem Statement

We model the fluorescence as a system of linear equations by considering each physical phenomenon [5]

$$Af + \varepsilon = b \tag{2}$$

where $b \in \mathbb{R}^m$ is a $m \times 1$ vector of measurements, $A \in \mathbb{R}^{m\times n}$ is an $m \times n$ coefficient matrix, $f \in \mathbb{R}^n$ is the $n \times 1$ vector of unknown Doppler (Gaussian) profile, and $\varepsilon \in \mathbb{R}^m$ is the $m \times 1$ measurement error/noise. A *well-posed* problem $Af = b$ where A is a normal operator in Hilbert space (complete) is defined by the Hadamard conditions: existence, uniqueness, and stability. A *well-posed* problem requires A to be objective and A^{-1} must be continuous [6]. In some cases, a unique solution may be difficult to find initially, especially for an overdetermined system. However, reformulating the problem using a least-squares approach yields a solution. On the other hand, an underdetermined system can have infinitely many solutions. A unique solution can be obtained using a minimum norm technique, but the stability of the solution is affected because a small amount of noise in the data amplifies the error. Also, we must pose the problem so that A^{-1} exists and is continuous. Otherwise, the solution does not depend on the data continuously. Actual results always include some variations in the measurements because of *ill-posedness*. The magnitude of variance can be determined from the product of the norm of A with its inverse norm, which defines *condition number* [7]

$$\text{cond}(A) = \|A\|_2\|A^{-1}\|_2 = \frac{d_1}{d_{\min\{m,n\}}} \tag{3}$$

where d_i is the ith singular number of matrix A.

III. Regularization Model

Regularization methods impose regularity on the solution by suppressing the noise level of an *ill-posed* inverse problem. The least-squares or minimum norm solution for a linear system requires an inversion of the forward model that maps the unknown signal to the data; however, the stability of the solution is affected because of the inherent noise. The inverse operation of the discrete linear problem can be *ill-posed*, which can produce a large error in the reconstruction, even for a small noise in the data.

A. Truncated SVD

For an *ill-posed* problem, a minimum-norm solution can satisfy the first two Hadamard conditions of a *well-posed* problem while using a pseudoinverse (Moore-Penrose inverse) of A. But, the solution's instability still exists, which can violate Hadamard's third condition. TSVD method can overcome the violation of Hadamard's condition and reconstruct the function. The SVD is the starting point for regularization techniques. The coefficient matrix A in (2) can be written in the expansion of SVD

$$A = UDV^T \tag{4}$$

where $U \in \mathbb{R}^{m\times m}$, $V \in \mathbb{R}^{n\times n}$ are orthonormal matrices, $D = \text{diag}(d_1, d_2, \ldots, d_{\min\{m,n\}}) \in \mathbb{R}^{m\times n}$ has nonnegative entries on the diagonal and zeros on the off-diagonal such that $d_1 \geq d_2 \geq \cdots \geq d_{\min\{m,n\}} \geq 0$. The least-squares solution

$$f_{\text{LS}} = A^{\dagger}b = \sum_{i=1}^{r} \frac{1}{d_i}\langle u_i^T, b\rangle v_i \tag{5}$$

where, $A^{\dagger} = VD^{\dagger}U^T = \sum_{i=1}^{r} v_i d_i^{-1} u_i^T$ is the pseudoinverse of A and $r = \text{rank}(A) \leq \min\{m, n\}$. Singular values decrease monotonically, leading to more oscillation (sign changes) of corresponding singular vectors $v_i \in V$ and $u_i \in U$. The noise in the measurements can affect the solution due to the small singular value in the denominator in (5), resulting in an unstable solution. The TSVD addresses this problem by filtering out the influences of smaller singular values by truncating the series to k. The TSVD solution can be written as

$$f_{\text{tsvd}}(b) = VD_k^{\dagger}U^T b = \sum_{i=1}^{k} \frac{1}{d_i}\langle u_i^T, b\rangle v_i \tag{6}$$

where $A_k^{\dagger} = VD_k^{\dagger}U^T$. All Hadamard's conditions hold: the single-valued linear mapping $f_{\text{tsvd}} : \mathbb{R}^m \to \mathbb{R}^n$ is well-defined, and the norm

$$\|f_{\text{tsvd}}\| = \left\|VD_k^{\dagger}U^T\right\| \leq \|V\|\left\|D_k^{\dagger}\right\|\|U^T\| = \left\|D_k^{\dagger}\right\| = (d_k)^{-1} \tag{7}$$

implies continuity. Simplifying (6) yields

$$\begin{aligned} f_{\text{tsvd}}(b) &= VD_k^{\dagger}U^T(Af + \varepsilon) \\ &= VD_k^{\dagger}(U^TU)DV^T f + VD_k^{\dagger}U^T\varepsilon. \end{aligned} \tag{8}$$

The first part of the right-hand side of (8) approximates f, while the second term associated with the error yields

$$\left\|VD_k^{\dagger}U^T\varepsilon\right\| \leq \left\|VD_k^{\dagger}U^T\right\|\|\varepsilon\| = \left\|D_k^{\dagger}\right\|\|\varepsilon\| = (d_k)^{-1}\|\varepsilon\|. \tag{9}$$

Since $d_1^{-1} \leq d_2^{-1} \leq \cdots \leq d_k^{-1}$, fewer singular values result in less noise amplification in the reconstruction. The quality of the solution depends on the optimum number of singular values.

B. Tikhonov

The idea of Tikhonov regularization is to minimize the expression $\|Af - b\|^2 + \alpha\|If\|^2$, where identity matrix I represents the regularization matrix, and $0 < \alpha < \infty$ denotes the regularization parameter [5], [6], [8]. The expression has two parts: data discrepancy or residual norm ($\|Af - b\|$) and solution norm or smoothing norm ($\|If\|$). The Tikhonov functional

$$J_\alpha(f) = \|Af - b\|^2 + \alpha\|If\|^2 \tag{10}$$

where $\nabla^2 J_\alpha(f) = 2(A^T A + \alpha I)$ is positive semidefinite. The solution is obtained by solving the system of the following equations:

$$\left(A^T A + \alpha I\right) f_{\text{tikh}} = A^T b \tag{11}$$

$$f_{\text{tikh}}(b) = \left(A^T A + \alpha I\right)^{-1} A^T b \tag{12}$$

where $A_{\text{tikh}} = (A^T A + \alpha I)^{-1} A^T$. Adding a positive number to the diagonal elements of the coefficients matrix results in instability. Using the SVD of matrix $A = UDV^T$

$$f_{\text{tikh}}(b) = V^{-T}\left[\left(D^2 + \alpha\right)^{-1} D\right] U^T b. \tag{13}$$

Orthogonality implies

$$f_{\text{tikh}}(b) = V\mathfrak{D}_\alpha U^T b \tag{14}$$

where the diagonal matrix, $\mathfrak{D}_\alpha = [(D^2 + \alpha)^{-1} D]$

$$\mathfrak{D}_\alpha = \text{diag}\left(\frac{d_1}{d_1^2 + \alpha}, \ldots, \frac{d_{\text{r}}}{d_r^2 + \alpha}, 0, 0, \ldots\right). \tag{15}$$

Simplifying (14) yields

$$f_{\text{tikh}}(b) = \sum_{i=1}^{r} g_i(\alpha) \frac{\langle u_i^T, b\rangle v_i}{d_i} \tag{16}$$

where $g_i(\alpha) = (d_i^2)/(d_i^2 + \alpha)$ is known as filter factors. The main goal is to remove the effects of small singular values. The filter factors yield

$$g_i(\alpha) \approx \begin{cases} 1, & \text{if } d_i \gg \sqrt{\alpha}, \text{ or } \alpha = 0 \\ 0, & \text{if } d_i \ll \sqrt{\alpha} \end{cases} \tag{17}$$

which are bounded, and $1 \geq g_1 \geq g_2 \geq \cdots \geq g_r \geq 0$. Filter factors close to one (for a larger singular value) reduce the SVD components of the residual. It is clear that for a negligible regularization parameter, the reconstruction (16) becomes a least-squares solution. For the TSVD

$$g_i(\alpha) = \begin{cases} 1, & \text{if } 1 \leq i \leq k \\ 0, & \text{if } k < i \leq r. \end{cases} \tag{18}$$

Smoothing the solution is one of the key tasks in any regularization method. Instead of using the identity matrix, we can write a general form using a suitable coefficient matrix L

$$f_{\text{tikh}}(b) = \arg.\min_{f \in \mathbb{R}} \left\{\|Af - b\|^2 + \alpha\|Lf\|^2\right\}. \tag{19}$$

Equation (19) is referred to as a generalized Tikhonov solution and $(A^T A + \alpha L^T L)^{-1} A^T$ is the generalized inverse. We apply a first-order finite difference matrix (first-order derivative operator) for the first-order Tikhonov

$$L = \begin{pmatrix} -1 & 1 & 0 & 0 & \cdots & 0 \\ 0 & -1 & 1 & 0 & \cdots & 0 \\ 0 & 0 & -1 & 1 & \cdots & 0 \\ \vdots & \cdots & \cdots & \ddots & \cdots & \vdots \\ 0 & \cdots & 0 & 0 & -1 & 1 \\ 0 & \cdots & 0 & 0 & 0 & -1 \end{pmatrix}. \tag{20}$$

While for second-order Tikhonov, we use a second-order derivative operator

$$L = \begin{pmatrix} 1 & -2 & 1 & 0 & \cdots & 0 \\ 0 & 1 & -2 & 1 & \cdots & 0 \\ 0 & 0 & 1 & -2 & \cdots & 0 \\ \vdots & \cdots & \cdots & \ddots & \cdots & \vdots \\ 0 & \cdots & 0 & 0 & 1 & -2 \\ 0 & \cdots & 0 & 0 & 0 & 1 \end{pmatrix}. \tag{21}$$

C. Parameter Estimation

The quality of the reconstruction of an unknown function of an inverse problem depends on the truncation parameter k (TSVD) and norm smoothing parameter α (Tikhonov regularization). An appropriate parameter produces the highest fidelity solution and does not impose oscillatory reconstruction due to noise amplification or over-smoothing reconstruction. Currently, no explicit unique method exists that estimates optimum parameters. For the LIF spectroscopy, we use L-curve and GCV methods to determine the regularization parameters effectively.

The L-curve method provides a quantifiable way of determining the quasi-optimal value of α. The method plots all possible α values for all possible residual and solution norms. The optimum value of α is found at the maximum curvature (corner of the L-curve) for $\log\|Lf\|_2$ as a function of $\log\|Af - b\|_2$. The smooth function of $\log\|Lf\|_2$ looks like the letter L. Fig. 1 shows a sample L-curve to estimate the regularization parameter.

The GCV method estimates regularization parameters by minimizing the GCV function [7]

$$\text{GCV} = \frac{\|Af_{\text{reg}} - b\|_2^2}{\left(\text{trace}\left(I - AA_{\text{reg}}\right)\right)^2} \tag{22}$$

where f_{reg} is the regularized solution such that $f_{\text{reg}} = A_{\text{reg}} b$. In the case of TSVD, $f_{\text{reg}} = f_{\text{tsvd}}$, and $A_{\text{reg}} = A_k^\dagger$. While for Tikhonov regularization, $f_{\text{reg}} = f_{\text{tikh}}$ and $A_{\text{reg}} = A_{\text{tikh}}$. Fig. 2 shows the GCV function used to estimate the truncation parameter.

IV. Error Analysis

The error in these regularization techniques comprises smoothing errors due to data loss and noise error (statistical variations) [6]

$$\text{err}_\alpha = \text{err}_{s\alpha} + \text{err}_{n\alpha}.\text{err}_{s\alpha} \tag{23}$$

$\text{err}_{s\alpha}$ represents error due to data loss, and $\text{err}_{n\alpha}$ denotes noise error. In a semi-random approach, the smoothing error is

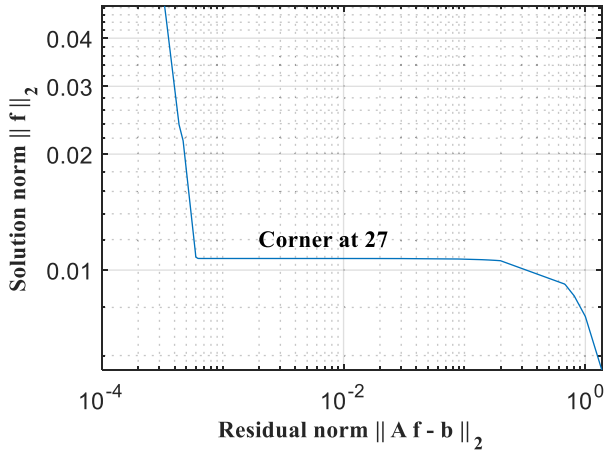

Fig. 1. Estimating truncation parameter using the L-curve method.

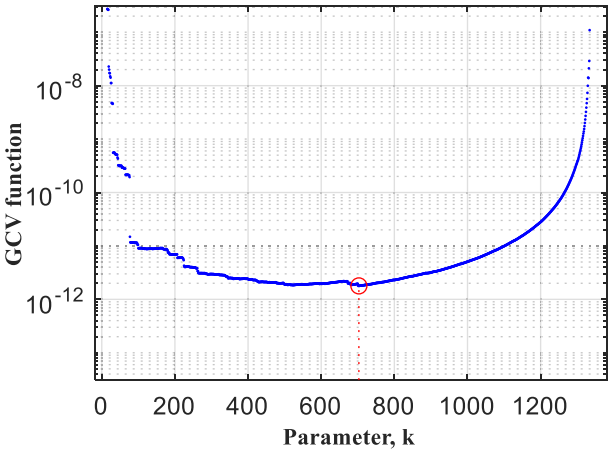

Fig. 2. Estimating truncation parameter using GCV.

deterministic, whereas the noise error is random and can have a zero mean and covariance. The expected value of the total error is defined as follows:

$$E\left\{\|\text{err}_\alpha\|^2\right\} = \|\text{err}_{s\alpha}\|^2 + E\|\text{err}_{n\alpha}\|^2 \tag{24}$$

where the expected value of the noise error is computed [10]

$$E\left\{\|\text{err}_{n\alpha}\|^2\right\} = d_i^2 \sum_{i=1}^{k} \left(\frac{d_i^2}{d_i^2+\alpha}\right) \frac{\|v_i\|^2}{d_i}. \tag{25}$$

The smoothing error increases and the noise error decreases with α. Since the exact solution f is unknown, the quality of the reconstruction cannot be determined. However, the relative errors when comparing the model data with measured data estimate the quality of the solution. We model fluorescence, m using the reconstructed Gaussian function. The relative error using the p-norm ($p = 1, 2, 3, \ldots, \infty$) is defined as

$$\text{Rel.err} = \frac{\|b-m\|_p}{\|Lf\|_p}.100\%. \tag{26}$$

V. Test Facility

The space propulsion laboratory at The University of Alabama has a vacuum test facility that can achieve a base pressure of 9.2×10^{-7} torr. The HET used in this study was a laboratory model with a power rating of 1.5 kW. The operating conditions of the thruster for this experiment are listed in Table I.

TABLE I
Thruster Operation Conditions

Anode flow rate [sccm]	15
Cathode flow rate [sccm]	3
Discharge potential [V]	180
Discharge current [A]	4.5
Keeper current [A]	1.25
Chamber pressure [torr]	2.2×10^{-5}

The thruster was modified to allow optical access. Two optical windows were placed in the discharge channel. The base plate of the thruster and anode had a window that allowed the laser to enter the discharge channel. Fluorescence was collected through the other window on the outer wall of the channel.

An extended-cavity tunable diode laser can scan wavelengths between 820 and 840 nm. The laser had a mode-hop-free range of 150 GHz at 834.955 nm. The laser was scanned from 359 079.63 to 359 024.63 GHz to promote Xe II electronic transition 5 $d[4]_{7/2} \rightarrow 6p[3]^0_{5/2}$ at 359 052.13 GHz. The maximum absorption of neutral xenon (Xe I) at 359 070.72 GHz, captured by a see-through hollow cathode lamp, provided a reliable reference. Fig. 3 shows the optical train outside the vacuum chamber.

A Faraday isolator was aligned with a laser beam to avoid back-reflection. The first beam splitter in the optical train (50–40) directed 50% of the laser (probe) beam through a chopper into an optical cable to obtain the beam inside the vacuum chamber. The remaining laser beam was used for reference and control of the experiment: 10% of the laser beam was fed into a wavemeter that monitored the wavelength and power, 10% of the beam passed through a Fabry–Perot etalon to monitor the quality of the scan, and 20% of the beam was directed through a chopper and then injected into a hollow cathode lamp filled with xenon. The lamp was the reference source, where Xe I atoms absorbed photons centered at a frequency of 359 070.72 GHz. The reference absorption was used to determine the Doppler shift and hence the velocity distribution. The center frequency of Xe II absorption is 18.58 GHz away from the center frequency of Xe I absorption (NIST). Fig. 4 shows the laser injection and fluorescence collection inside the discharge channel.

The probe beam entered the discharge channel of the thruster through a 2.5 mm window in the thruster's base plate. The laser beam was directed in the z-direction parallel to the electric field and perpendicular to the applied radial magnetic field. The fluorescence was collected by a collection of lenses (75 mm diameter and 250 mm focal length) orthogonal to the laser beam. A single-core fiber cable carried the fluorescence signal from the vacuum chamber back to the optical table (see Fig. 3).

The signal was directed through a monochromator (Horiba microHR) with a focal length of 140 mm and image magnification of 1:1 at the exit slit.

The monochromator grating position was set to the center wavelength of the expected fluorescence. The monochromator wavelength accuracy was ±0.25 nm for a 1200 gr/mm grating at 400 nm. The monochromator signal was then detected using a photomultiplier tube (PMT). The PMT signal was phased with the chopper frequency using a lock-in amplifier to separate the fluorescence signal from the background noise.

VI. Line Shape Broadening

The initial state of the Xe II transition, $5d[4]_{7/2}$ is a metastable state; therefore, it has a high population density and a long lifetime. The decay transition $6p[3]^0_{5/2} \rightarrow 6\,s[2]_{3/2}$ emits photons at 542 nm (vac). Isotopes producing Hfs splitting (xenon atomic mass of 129 and 131) are naturally abundant and listed in Table II. The upper excited state, $6p[3]^0_{5/2}$ has a robust non-resonant transition (with little to no photon scattering). Currently, the known Hfs splitting constants of xenon are limited to a specific set of energy levels. For this particular transition, the Hfs constants of the upper excited state are available; however, the information is unknown for the lower excited state. Previous work suggested using published data for Hfs for a similar transition of $5d[D]_{7/2} \rightarrow 6p[P]_{5/2}$ [11].

The Doppler shift is a frequency shift caused by the thermal motion of atoms and molecules. If the atom emits a photon at a frequency ϑ_0, the observed frequency, ϑ can be shifted due to the relative motion away/toward

$$\vartheta = \vartheta_0 \pm \vartheta_0\left(\frac{v_z}{c}\right) \tag{27}$$

where, v_z is the speed of species along the z-direction, and c is the speed of light. Photons with frequencies below the center frequency (+ sign) move in the direction of the laser beam. A Gaussian function is used to determine temperature (28).

This relationship provides a robust approach for determining the plasma temperature by fitting the curve to the shape of the Doppler profile

$$\varphi_D(\vartheta) = \frac{c}{\vartheta_0}\left(\frac{M}{2\pi kT}\right)^{1/2} \exp\left[-\frac{Mc^2}{2kT}\left(\frac{\vartheta-\vartheta_0}{\vartheta_0}\right)^2\right] \tag{28}$$

where M is the mass of species, k is the Boltzmann constant and T is the species temperature. The species transfers to different energy states, and a photon is absorbed (increasing energy state) or emitted (returning to a lower energy state). The Heisenberg uncertainty principle sets the lifetime limit for the excited states. The limit is the relaxation time of a given species for a specific transition period. The limit also results in a frequency shift of photons from the spectral line values. This phenomenon causes spectral line broadening, which is referred to a natural lifetime broadening, defined by

$$\Delta\vartheta_{\text{nat}} = \frac{1}{2\pi\tau_u} \tag{29}$$

where τ_u denotes the radiative lifetime of the upper state. The Lorentzian function best describes the natural lifetime broadening

$$\varphi_L(\vartheta-\vartheta_0) = \frac{1}{\pi}\frac{\Delta\vartheta_{\text{nat}}/2}{(\vartheta-\vartheta_0)^2 + \left(\frac{\Delta\vartheta_{\text{nat}}}{2}\right)^2}. \tag{30}$$

The radiative lifetime of the upper state is inversely reciprocal to Einstein's A coefficient, which is $6.2 \times 10^7(\text{s}^{-1})$ (NIST).

The linear Zeeman effect caused by the applied magnetic field distorts (splits) the fluorescence line shape. The strength of the radial magnetic field varies with the axial and radial locations of the thruster. Therefore, the magnitude of the Zeeman effect on the fluorescence line shape is also dependent on the axial position. For the Xe II $5d[4]_{7/2} \rightarrow 6p[3]^0_{5/2}$ transition, π-Zeeman splitting effects are negligible, but σ-Zeeman splitting effects still exist [12]. The Zeeman effect in moderate magnetic field strengths (∼145 G for our experiment) can contribute several hundred MHz to the overall LIF. The contribution of this effect is significantly less than that observed from collisional or Doppler broadening and is difficult to discern.

VII. Results and Discussion

The Doppler shift of the bulk motion of the plasma in the HET is related to the potential drop. The potential drop from anode voltage to beam potential along the length of the chamber is affected mostly by ionization and acceleration. The exit velocity of the ions depends on the axial location (voltage potential) in the channel when the particle ionizes. Additionally, the amount of noise in the fluorescence signal varies with the axial location of the thruster. The fluorescence signal can exhibit multiple peaks and long tails with significant variance in the near exit plane, meaning that Xe II ions are not all in the same energy state, contributing greatly to the variability in velocity. The magnetic field is designed to focus on the plume, often creating regions with bimodal fluorescence measurements.

The numerical model in (2) requires a set of initial values. A point spread function (PSF) has been proven insightful in previous studies. We developed a PSF from the right-hand side of (1) resulting from known Hfs (isotopes), natural lifetime broadening, and their appropriate spectral ranges in the fluorescence data. Before applying the regularization methods, the Savitzky–Golay data smoothing algorithm was applied to the raw fluorescence data to best represent the spectral response without removing significant statistical variations. We collected LIF signals every millimeter inside the discharge channel along the centerline from the top of the anode to the exit of the channel and the plume. Although all collected fluorescence was investigated thoroughly with these regularization methods, in this study, we presented fluorescence data for Xe II collected at a 21 mm location along the axial z-direction (see Fig. 5).

The dimension of the Gaussian function was determined by the frequency range of the scan and the laser resolution. We estimated the condition number of 145 841.83, suggesting a severely *ill-posed* problem. The decay of the singular values is shown in Fig. 6.

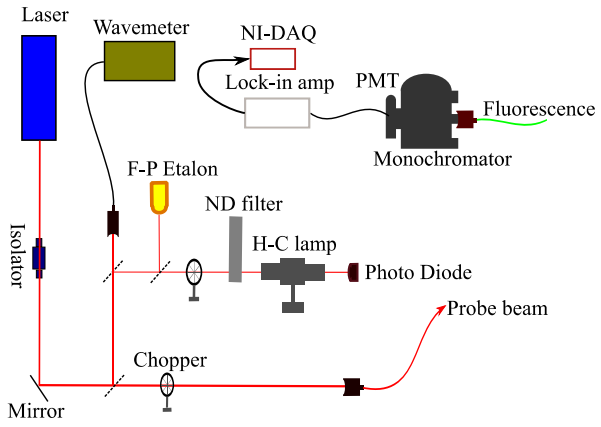

Fig. 3. LIF optical setup outside the chamber.

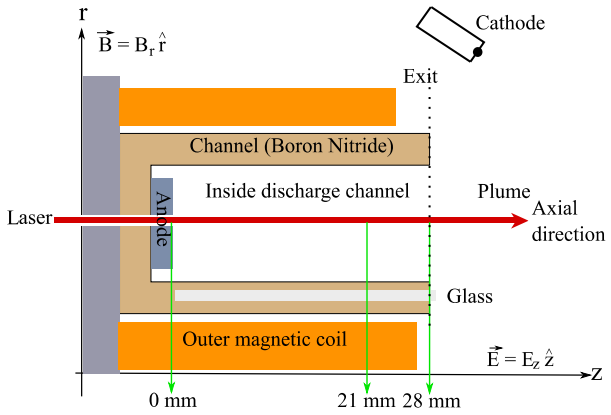

Fig. 4. Laser path and fluorescence collection in the discharge channel.

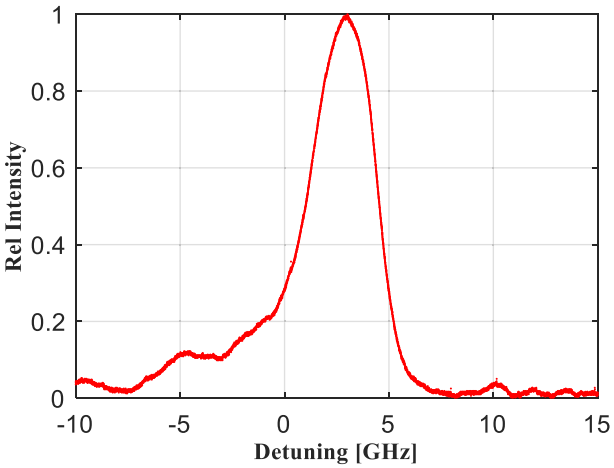

Fig. 5. Raw LIF signal.

The importance of the technique can be analyzed by comparing measured fluorescence with Gaussian reconstruction with and without regularization. Fig. 7 shows the reconstruction of the Gaussian function using the TSVD with GCV and L-curve methods, all singular values, and without regularization.

The reconstruction using all singular values shows a very wavy structure resulting in an impractical Gaussian function and width. The reconstruction without applying the regularization method reveals broader Gaussian width, resulting

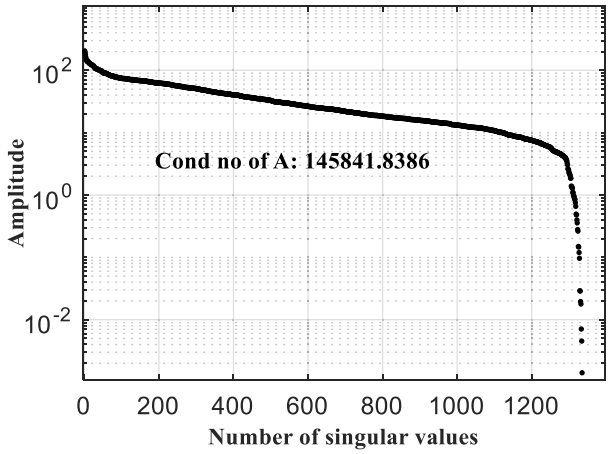

Fig. 6. Singular value spectrum.

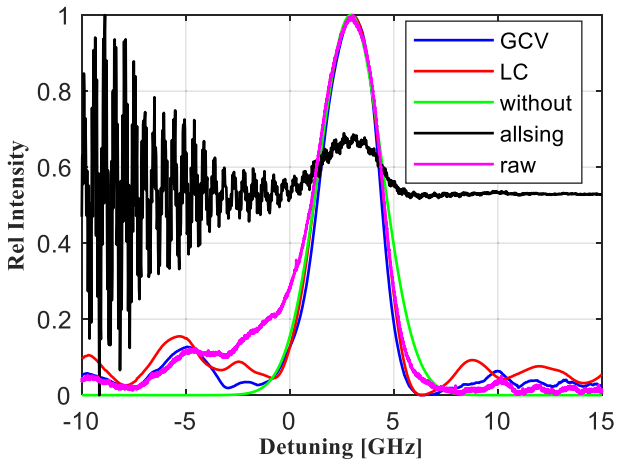

Fig. 7. Gaussian reconstructions: raw signal (magenta), TSVD with GCV (blue) and L-curve (red), using all singular values (black), and without applying regularization (green).

in higher ion temperature. The augmented temperature is about 8290 K. Fig. 8 shows the reconstructions using the GCV method and a comparison with the raw fluorescence signal.

Tikhonov's second-order method provides a little oscillatory solution in the range of $(-10, -3)$ GHz; nevertheless, all technique offers a good reconstruction. Finding the peak position is essential for determining the Doppler shift and hence the velocity distribution of Xe II. The reconstructions using Tikhonov zeroth-order and TSVD methods provide ambiguous peak positions compared to Tikhonov first-order. A similar reconstruction is found when the L-curve method is applied, Fig. 9.

Tikhonov zeroth-order provides an oscillatory reconstruction with an ambiguous peak while TSVD overestimates the Doppler profile. Tikhonov's first and second-order methods return better reconstruction, but the optimum value of the parameter α is not found at the maximum curvature of the L-curve; Fig. 10.

The L-curve method for Tikhonov regularization tends to produce regularization parameters slightly over-smooth. If the SVD coefficients decay faster to zero such that the first few SVD components dominate the solution, the L-curve criteria may fail [13]. The resulting temperatures for these four methods are relatively similar and listed in Table III.

TABLE II
THRUSTER OPERATION CONDITIONS

Isotope	124_{Xe}	126_{Xe}	128_{Xe}	129_{Xe}	130_{Xe}	131_{Xe}	132_{Xe}	134_{Xe}	136_{Xe}
Abundance	0.09	0.09	1.29	26.44	4.08	21.18	26.89	10.44	8.87
Spin	0	0	0	1/2	0	3/2	0	0	0

TABLE III
THRUSTER OPERATION CONDITIONS

Methods	GCV	L-curve
TSVD	16,301	17,611
Tikhonov: Zeroth	16,310	16,307
Tikhonov: First	16,302	16,308
Tikhonov: Second	16,305	16,301
Without Regularization	24590	

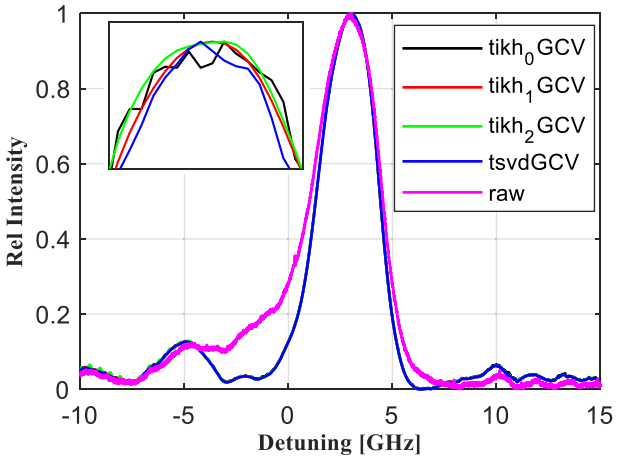

Fig. 8. Gaussian reconstructions using GCV method: raw signal (magenta), Tikhonov zeroth-order (black), Tikhonov first-order (red), Tikhonov second-order (green), and TSVD (blue).

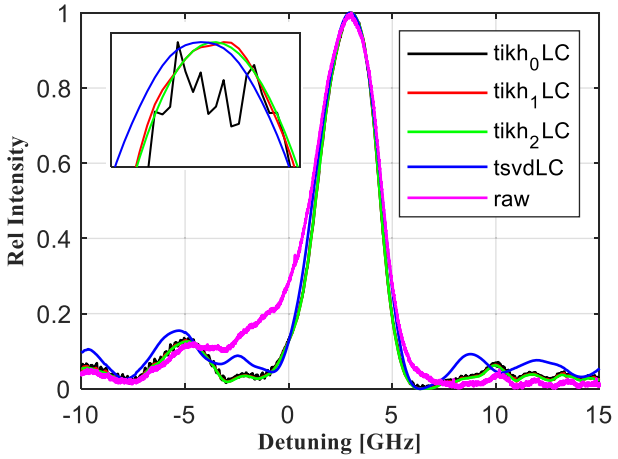

Fig. 9. Gaussian reconstructions with L-curve method: raw signal (magenta), Tikhonov zeroth-order (black), Tikhonov first-order (red), Tikhonov second-order (green), and TSVD (blue).

The average ion temperature is approximately 16 303 K. In contrast, without applying the regularization, the corresponding ion temperatures increase up to 24 590 K.

We also estimated the Doppler shift of about 3.02 GHz, resulting in exhaust velocities of 2.52 km/s. It is worth noting that the typical ion exhaust velocity is approximately 20.0 km/s in the plume for a moderate discharge condition.

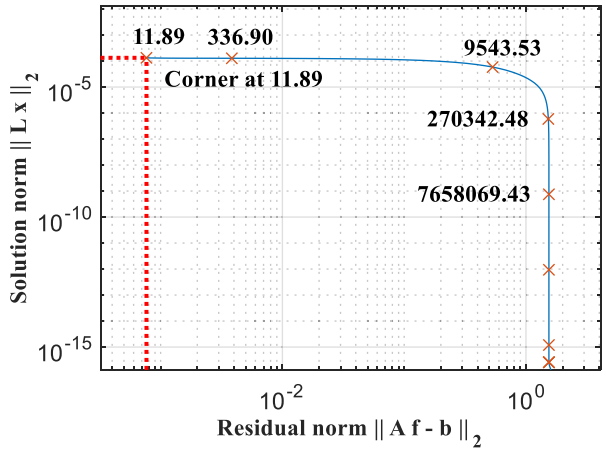

Fig. 10. L-curve of Tikhonov first-order method.

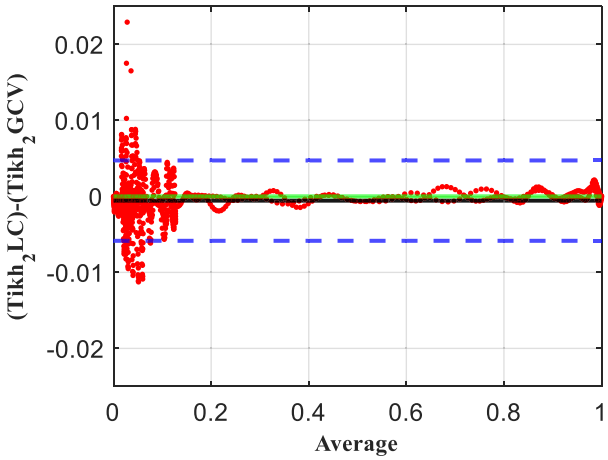

Fig. 11. Method comparison between L-curve and GCV of Tikhonov second-order.

Ions produced at different axial locations experience different plasma potential drops. The plasma potential varies along the axial z-direction, resulting in various Doppler shifts. In the HET, Xe II downstream (away from the anode) experiences greater acceleration due to the higher electric potential, resulting in a much larger Doppler shift in the LIF response.

We observed that the reconstructed Gaussian profiles are not ideal Gaussian functions for all cases. A noticeable side peak at around -4.75 GHz suggests a fraction of the ion population with a distinct energy level is substantially shifted from the center frequency. As the second population of ions becomes more significant at higher discharge powers, the model needs to be extended to two-temperature Gaussian functions; otherwise, the accuracy of the model will suffer.

Quantifying the total error is difficult without a verifiable and independent method to determine the temperature conclusively. Statistical techniques can analyze the quality of these methods, though. Correlation can be assessed by calculating the difference between two measurements and comparing the

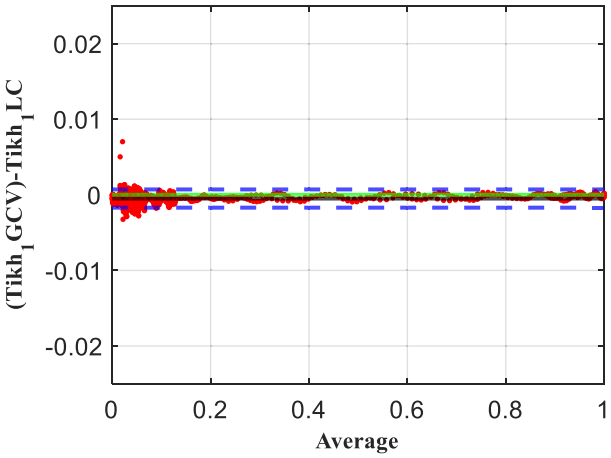

Fig. 12. Method comparison between L-curve and GCV of Tikhonov first-order.

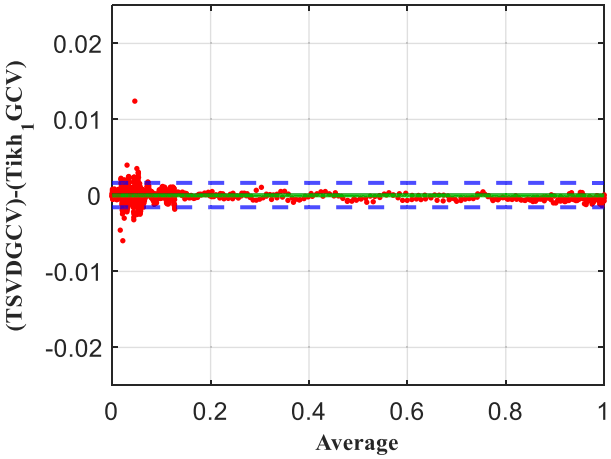

Fig. 13. Method comparison between TSVD and Tikhonov first-order using GCV method.

trend line with the line of identity. The Bland-Altman plot uses the differences between the two methods along the y-axis and their averages along the x-axis and quantifies the significance of systematic and proportional errors [14]. We conducted the comparisons and presented them in Figs. 11–13. The red dots represent the difference between the two methods, whereas the green and black lines correspond to the line of equality and bias, respectively. The bias measures the trade-off between the difference from the line of equality. The line of equality ideally indicates no differences between the measurements. In addition, a 95% confidence interval to the bias defines the limits of agreement between the methods and presents in blue dashed lines; the smaller the width better the agreement. The comparison of the reconstruction using the L-curve and GCV method for the Tikhonov second-order is shown in Fig. 11. A broader limit of agreement is observed, suggesting less agreement between the methods.

The differences are widely distributed, and the degree of variability is inconsistent. These results reinforce the idea that significant systematic differences exist between these methods. However, a relatively small difference between L-curve and GCV methods for Tikhonov first-order is observed, Fig. 12. The limit of agreement is relatively narrow, smaller bias still exists though.

TABLE IV
THRUSTER OPERATION CONDITIONS

Error [%]	TSVD	$Tikh_1$
L^1	8.80	8.06
L^2	5.14	4.73
L^3	2.24	2.07

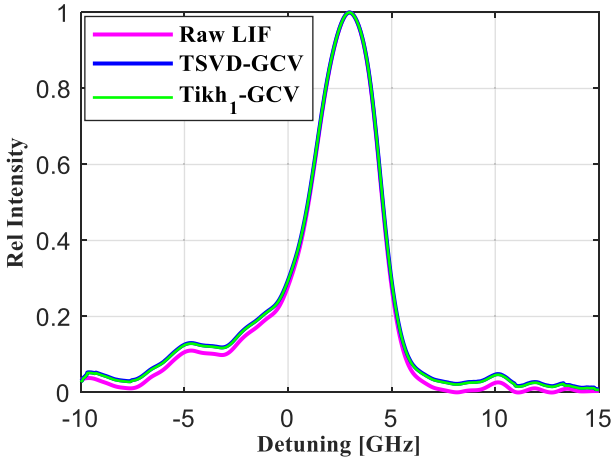

Fig. 14. Comparison between measured and model data: raw LIF (magenta), TSVD with GCV (blue), and Tikhonov first-order with GCV (green).

The reconstructions using these two methods are independent and comparable. Nevertheless, a better result is found for the GCV method used in Tikhonov's first-order and TSVD techniques in Fig. 13.

We observed almost no statistical bias. The magnitude of the differences is relatively small compared to the other comparisons and is distributed around the line of equality. Despite the 95% confidence interval being larger than Fig. 12, it is relatively smaller and the statistical bias is negligible, resulting in better agreement between the methods. We modeled the fluorescence signals using these two methods, which approximated the measured fluorescence (see Fig. 14).

The estimated relative errors between the model fluorescence and measured (smooth) fluorescence are listed in Table IV.

TSVD and Tikhonov first-order using the GCV method are reliable and provide a similar temperature. But, the quality of reconstruction and errors suggest Tikhonov's first-order with GCV method is the better approach.

VIII. LIF VALIDATION

Estimating Xe II temperature using other methods validates LIF measurements. We estimated Xe I temperature from LIF and thermocouple measurements since direct measurement of Xe II temperature other than LIF is limited. The annular-shaped anode injects Xe I propellant through several small orifices (diameters less than 1 mm) in the axial direction. Since the anode heats Xe I, the expected Xe I temperature is to be higher than room temperature [15]. The anode is heated by the discharge current and cooled using the mass flow rate. The expected values are between 800 and 1000 K at a moderate discharge voltage of 300 V [16]. The anode

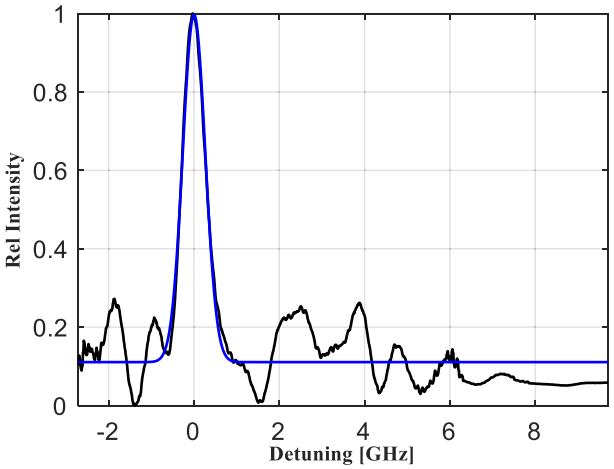

Fig. 15. Xe I LIF. Gaussian reconstruction (black) and Lev-Marq curve fitting (blue).

temperature was measured using a K-type thermocouple at approximately 674 K at a discharge voltage of 160 V. The laser was capable of pumping the electronic transition $6\,s^2[1/2]^0_1 \rightarrow 6p^2[3/2]_2$ at 834.68 nm to excite Xe I. The decay transition $6p^2[3/2]_2 \rightarrow 6\,s^2[3/2]^0_1$ emits fluorescence at 473.41 nm. Xe I LIF measurement was performed just above the anode surface ($\sim$1.0 mm). We estimated the Xe I temperature of 752 K using the Tikhonov first-order with GCV method, Fig. 15.

The difference between the LIF results and the measured values was within 10%. The results require further investigation of the discrepancy between the two values but provide confidence in our regularization technique.

IX. Conclusion

The Tikhonov first-order and TSVD employing the GCV method provide better performance for our problem. Compared to the test case (measured values), these two approaches return accurate reconstruction within 2.0%–8.0% of the actual measurements. These two methods provide consistent ion temperatures and best represent the underlying physics.

Tikhonov zeroth-order and TSVD approaches result in ambiguous peak positions, bringing the solution's validity into question. The GCV method resembles a reasonably better approach for estimating the parameters, but a definitive method is required to estimate the regularization parameters.

The L-curve method for Tikhonov regularization tends to produce a slightly over-smoothed reconstruction. If the SVD coefficients decay faster to zero such that the first few SVD components dominate the solution, the L-curve criteria may fail. The L-curve method requires solving the minimization problem several times to determine the optimum α, enabling computationally more expensive than the GCV approach.

References

[1] R. J. Cedolin, W. A. Hargus Jr., P. V. Storm, R. K. Hanson, and M. A. Cappelli, "Laser-induced fluorescence study of a xenon Hall thruster," *Appl. Phys. B, Lasers Opt.*, vol. 65, pp. 459–469, Oct. 1997.

[2] D. Keefer, N. Wright, J. O. Hornkohl, and J. Bangasser, "Multiplexed LIF and Langmuir probe diagnostic measurements in the TAL D-55 thruster," in *Proc. 35th Joint Propuls. Conf. Exhibit*, Los Angeles, CA, USA, 1999, p. 2425.

[3] T. B. Smith, "Deconvolution of ion velocity distributions from laser-induced fluorescence spectra of xenon electrostatic thruster plumes," Ph.D. dissertation, Dept. Aerosp. Eng., Univ. Michigan, Ann Arbor, MI, USA, 2003.

[4] W. A. Hargus and M. R. Nakles, "Evolution of the ion velocity distribtuion in the near field of the BHT-200-X3 Hall thruster," in *Proc. 42nd AIAA/ASME/SAE/ASEE Joint Propuls. Conf. Exhibit*, Sacramento, CA, USA, 2006, p. 4991.

[5] J. L. Mueller and S. Siltanen, *Linear and Nonlinear Inverse Problems With Practical Applications*, 1st ed. Philadelphia, PA, USA: SIAM, 2012.

[6] A. Neumaier, "Solving ill-conditioned and singular linear systems: A tutorial on regularization," *SIAM Rev.*, vol. 40, no. 3, pp. 636–666, 1998.

[7] P. C. Hansen, *Fundamentals of Algorithms Discrete Inverse Problems: Insight and Algorithms*. Philadelphia, PA, USA: SIAM, 2010.

[8] S. Pereverzev and E. Schock, "Morozov's discrepancy principle for Tikhonov," *Numer. Funct. Anal. Optim.*, vol. 21, nos. 7–8, pp. 901–916, Jan. 2000.

[9] P. C. Hansen, "Analysis of discrete ill-posed problems by means of the L-curve," *SIAM Rev.*, vol. 34, no. 4, pp. 561–580, Dec. 1992.

[10] A. Doicu, T. Trautmann, and F. Schreier, *Numerical Regularization for Atmospheric Inverse Problems*, 1st ed. Berlin, Germany: Springer-Verlag, 2010.

[11] D. Manzella, "Stationary plasma thruster ion velocity distribution," in *Proc. 30th Joint Propuls. Conf. Exhibit*, Indianapolis, IN, USA, 1994, pp. 1–13.

[12] W. Huang, B. Drenkow, and A. D. Gallimore, "Laser-induced fluorescence of singly-charged xenon inside a 6-kW Hall thruster," in *Proc. 45th AIAA/ASME/SAE/ASEE Joint Propuls. Conf. Exhibit*, Denver, CO, USA, 2009, pp. 1–23.

[13] M. Hanke, "Limitations of the L-curve method in ill-posed problems," *BIT Numer. Math.*, vol. 36, no. 2, pp. 287–301, Jun. 1996.

[14] J. M. Bland and D. G. Altman, "Statistical methods for assessing agreement between two methods of clinical measurement," *Lancet*, vol. 327, no. 8476, pp. 307–310, Feb. 1986.

[15] B. M. Reid, "The influence of neutral flow rate in the operation of Hall thrusters," Ph.D. dissertation, Dept. Aerosp. Eng., Univ. Michigan, Ann Arbor, MI, USA, 2009.

[16] C. F. Book and M. L. R. Walker, "Effect of anode temperature on Hall thruster performance," *J. Propuls. Power*, vol. 26, no. 5, pp. 1036–1044, Sep. 2010.

A. K. M. Mustafizur Rahman received the Ph.D. degree in aerospace engineering and mechanics from The University of Alabama, Tuscaloosa, AL, USA, in 2023.

His current research interests include plasma thrusters (Hall/ion thruster), laser-induced fluorescence, electric probes, and low-temperature plasmas.

Richard Branam received the Ph.D. degree from The Pennsylvania State University, State College, PA, USA, in 2005.

His first faculty appointment was at the Air Force Institute of Technology (AFIT), Wright-Patterson Air Force Base, OH, USA. He has worked with NASA and the Air Force on several collaborative projects. He teaches and researches several areas of space propulsion. His laboratory actively investigates plasma thrusters, cathodes, and laser diagnostics. He joined the faculty at The University of Alabama, Tuscaloosa, AL, USA, in 2014, after 25 years in the Air Force, where he served as a Researcher and an Engineer. His Air Force career has provided him with many unique experiences in the areas of space propulsion, systems engineering, and program management. He has published research on rocket engines, combustion, laser diagnostics, hypersonics, space propulsion, and plasma dynamics.